

Yttrium- and nitrogen-doped NiCo phosphide nanosheets for high-efficiency water electrolysis

Guangliang Chen¹ | Huiyang Xiang² | Yingchun Guo¹ | Jun Huang³ | Wei Chen³ | Zhuoyi Chen² | Tongtong Li² | Kostya (Ken) Ostrikov⁴

¹Department of Materials Engineering, Huzhou University, Huzhou, China

²School of Materials Science and Engineering, Zhejiang Sci-Tech University, Hangzhou, China

³School of Physics and Electronic Information, Gannan Normal University, Ganzhou, China

⁴School of Chemistry and Physics, Centre for Materials Science, Centre for Clean Energy Technologies and Practices, Centre for Waste-Free World, Queensland University of Technology (QUT), Brisbane, Queensland, Australia

Correspondence

Guangliang Chen, Department of Materials Engineering, Huzhou University, 313000 Huzhou, China.
 Email: glchen@zjhu.edu.cn

Tongtong Li, School of Materials Science and Engineering, Zhejiang Sci-Tech University, 310018 Hangzhou, China.
 Email: ytaji@zstu.edu.cn

Funding information

National Natural Science Foundation of China, Grant/Award Number: 52177162; the Natural Science Foundation of Zhejiang Province, Grant/Award Numbers: LZ22E070003, LQ22E020006; the Funding Project for Academic/Technical Leaders of Jiangxi Province, Grant/Award Number: 20225BCJ22003; the Natural Science Foundation of Jiangxi Province, Grant/Award Number: 20212ACB211001

Abstract

Engineering high-performance and low-cost bifunctional catalysts for H₂ (hydrogen evolution reaction [HER]) and O₂ (oxygen evolution reaction [OER]) evolution under industrial electrocatalytic conditions remains challenging. Here, for the first time, we use the stronger electronegativity of a rare-Earth yttrium ion (Y³⁺) to induce in situ NiCo-layered double-hydroxide nanosheets from NiCo foam (NCF) treated by a dielectric barrier discharge plasma NCF (PNCF), and then obtain nitrogen-doped YNiCo phosphide (N-YNiCoP/PNCF) after the phosphating process using radiofrequency plasma in nitrogen. The obtained N-YNiCoP/PNCF has a large specific surface area, rich heterointerfaces, and an optimized electronic structure, inducing high electrocatalytic activity in HER (331 mV vs. 2000 mA cm⁻²) and OER (464 mV vs. 2000 mA cm⁻²) reactions in 1 M KOH electrolyte. X-ray absorption spectroscopy and density functional theory quantum chemistry calculations reveal that the coordination number of CoNi decreased with the incorporation of Y atoms, which induce much shorter bonds of Ni and Co ions and promote long-term stability of N-YNiCoP in HER and OER under the simulated industrial conditions. Meanwhile, the CoN-YP₅ heterointerface formed by plasma N-doping is the active center for overall water splitting. This work expands the applications of rare-Earth elements in engineering bifunctional electrocatalysts and provides a new avenue for designing high-performance transition-metal-based catalysts in the renewable energy field.

KEY WORDS

overall water splitting, plasma etching, plasma N-doping, rare-earth electrocatalyst, yttrium incorporation

1 | INTRODUCTION

Hydrogen energy is widely used as a clean energy source,^{1,2} which has excellent potential to mitigate the global energy and environmental challenges facing humankind. Currently, water splitting by electrolysis using renewable energy is considered as one of the most effective approaches for clean energy conversion and storage by providing high-purity H₂ for hydrogen fuel cells. The main challenge in terms of water electrolysis lies in the design of efficient electrocatalysts to reduce the high overpotentials of the two half-reactions (hydrogen evolution reaction [HER] and oxygen evolution reaction [OER]), thereby speeding up the reactions.³ Although noble metal Pt and Ru/Ir-based catalysts are still the most effective electrocatalysts for HER and OER, respectively, their scarcity and high cost greatly limit commercial applications. Therefore, engineering abundant, low-cost, efficient, and stable nonnoble metal electrocatalysts is crucial for the development of H₂ energy.

It is well known that rare-Earth metals have excellent physical, chemical, optical, and electrical properties due to the presence of unfilled 4f electron orbitals.⁴ Among them, the 5d orbital available in the electronic structure of yttrium (Y) is empty, which can be used for electron transfer for catalytic reactions, while the robust catalytic activity of catalysts containing Y can be achieved by utilizing the well-known ability of Y to induce both oxidation and reduction. Furthermore, the addition of the Y element can also improve the mechanical strength, electrical conductivity (e.g., in superconducting materials), and thermal stability of catalysts.^{5,6} Noticeably, Y-based materials have been used in catalytic applications such as methyl orange degradation, hydrodesulfurization, and organic polymerization.⁷ However, water electrolysis using Y atom-containing catalysts has rarely been reported. Therefore, it is promising to use inexpensive Y as alternatives to precious metals in fabricating electrocatalysts for water splitting.

Transition-metal phosphides (TMPs) are promising as HER electrocatalysts, and the presence of phosphorus (P) can dilute the metal atoms while maintaining the electronic structure, thereby decreasing the free energy of adsorption of hydrogen atoms.^{8,9} In addition, due to the weak electronegativity of P, the confinement effect of free electrons for metal atoms is limited, endowing many TMPs with good electrical conductivity, so that some metal-rich phosphides can show superconducting properties.¹⁰ As the most common Ni and Co TMP, the engineered NiCoP_x shows higher electrical conductivity, more efficient Faradaic redox reactions, and better stability to achieve substantially improved electrochemical

performance than their monometallic counterparts.¹¹ While significant progress has been made in terms of the HER performance of TMPs, their overall catalytic water-splitting (including the OER) performance needs to be improved significantly for their use in industrial applications.¹² Plasma, being the fourth state of matter along with solid, liquid, and gaseous states,¹³ has many advantages for engineering electrocatalysts, for example, in boosting the interfacial coupling between the catalyst and catalytic support materials,¹⁴ achieving effective heteroatom doping at much lower temperatures, etc.^{15,16} In our previous work,¹⁰ N-doped NiCo phosphides fabricated using a radiofrequency (RF) N₂ plasma showed high performance for both HER and OER reactions in an alkaline medium, making them promising for use as an electrode for industrial electrolysis. Based on the above discussion, combining rare-Earth metal Y, Ni, and Co transition metals, and plasma processing may be a new effective approach for in situ synthesis of custom-designed industry-relevant electrocatalysts for water electrolysis. To our knowledge, no similar studies have been reported to date, and this work may provide a new avenue of research for the advancement of clean H₂ energy technologies.

Herein, NiCo alloy foam is first modified by a dielectric barrier discharge (DBD) plasma to form macro–nano defects on the NiCo foam (NCF) surface, and then a smooth ultrathin nanosheet of YNiCo lactate dehydrogenase (LDH) is sprouted in situ from the plasma-modified NCF (PNCF), thus forming YNiCo LDH/PNCF structures at a relatively low hydrothermal temperature (180°C), which is very helpful for decreasing the crystal property of the resulting electrocatalyst.¹⁷ Finally, N-doped YNiCo phosphide (N-YNiCoP) is obtained by N₂-P RF plasma processing at a temperature of 550°C. Notably, the heteroatom doping and multiple-phase interfaces formed expose abundant active sites; meanwhile, the hydrophilic interface facilitates the transfer and diffusion of electrolytes and bubbles. X-ray absorption spectroscopy (XAS) results and density functional theory (DFT)-based quantum chemistry calculations reveal that the addition of Y³⁺ not only induces the growth of ultrathin Ni–Co nanosheets but also regulates the electronic structure and contributes to the regulation of energy for hydrogen adsorption. Besides, the heterogeneous interfaces formed between different phases also greatly promote the kinetics of HER and OER in basic media. Therefore, the optimized N-YNiCoP/PNCF structure shows extraordinary catalytic activity in 1 M potassium hydroxide (KOH), and it can achieve ultralow overpotentials of 252 and 331 mV for HER and 412 and 464 mV for OER at high and industry-relevant current densities of 1000 (j_{1000}) and 2000 (j_{2000}) mA cm⁻²,

respectively. Meanwhile, the HER current density-time test is performed for 200 h, and excellent reaction stability and catalyst durability are achieved. Furthermore, the dual-electrode system using both N-YNiCoP/PNCF||N-YNiCoP/PNCF as electrodes shows higher catalytic activity in the overall water splitting than that using the benchmark Pt/C/PNCF||RuO₂/PNCF catalyst. The results of this work fill the knowledge gap of application of Y-incorporated catalytic and plasma systems in the field of bifunctional water electrolysis for generating H₂ and O₂ in a sustainable, efficient, and stable manner.

2 | EXPERIMENTAL SECTION

2.1 | Chemicals and reagents

Bimetallic Ni–Co foams (NCF, 1-mm thick, Ni/Co ratio 1:9) were supplied by Suzhou Taili Mater. Tech. Co. Acetone, deionized water, anhydrous ethanol, HCl, Y(NO₃)₃·6H₂O (yttrium nitrate hexahydrate), ammonium fluoride (NH₄F, purity 98%), red P (98.5%), urea, and KOH were supplied by Hangzhou Mick Chem. Instr. Co. N₂, with 99.99% purity, was procured from Hangzhou Jingong Special Gas Co. The reagents used in this work were all of analytical grade.

2.2 | PNCF fabrication

To prepare the substrate, NCF foam (2 × 2 cm) was cleaned by 6 min of ultrasonication (60 W) in acetone reagent and HCl (1 M) solution. Thereafter, the foam was cleaned five times using anhydrous ethanol and deionized water, and then oven-dried at a temperature of 60°C for 10 min. Subsequently, both NCF surfaces were processed using a DBD plasma discharge in air operated for 5 min with an AC power of 60 W. As a result, the plasma-modified NCF (PNCF) substrate was obtained.

2.3 | In situ fabrication of YNiCo LDH/PNCF

First, 0.156 mmol of Y(NO₃)₃·6H₂O, 5 mmol of urea, and 2.5 mmol of NH₄F were dissolved in 20 mL of deionized water; a magnetic stirrer was used for 15 min until a homogeneous flocculent medium was formed. Then, the mixture and PNCF were placed in a reaction autoclave lined with Teflon (30 mL) and kept at 180°C for over 10 h. Upon cooling of the kettle to 40°C, samples were cleaned five times using deionized water and ethanol. Subsequently, YNiCo LDH/PNCF was heated for 30 min

(at 50°C) in a conventional oven. To obtain the optimum YNiCo LDH/PNCF catalyst, various parameters were also investigated in this work.

2.4 | Synthesis of N-YNiCoP/PNCF using plasma

In the plasma-enhanced chemical vapor deposition (PECVD) reactor, YNiCo LDH/PNCF samples and 0.2 g of red P in powder form were placed downstream and upstream of the vessel made of porcelain, respectively. Two Cu electrodes with circular shapes were wound around a quartz-made tube connected to a 500 W RF (RF: 13.56 MHz) source (Microelectronics Center, CAS, type SY) to generate the plasma. Afterward, the specimens were heated up to 550°C (at a heating rate of 5°C min⁻¹) and exposed to P + N₂ plasma for over 2 h. The discharge power was 100 W, and the pressure was 2.5 Pa. After the process of phosphorizing, the N-doped YNiCo phosphide specimens were cooled down to 25°C at a N₂ flow rate of 20 sccm, which was labeled as N-YNiCoP/PNCF. To optimize the electrocatalytic performance, various process parameters for the synthesis of an N-YNiCoP/PNCF catalyst were studied as well. It should be noted that the N-doping achieved by the N₂-RF plasma is a green and low-temperature protocol, which is very helpful for increasing the electrocatalytic performance of N-YNiCoP/PNCF. Briefly, the RF plasma is used to dissociate the N₂ molecules into N atoms and other chemical bonds, which in turn induces heteroatom doping in the phosphating process.

2.5 | Fabrication of Pt/C/PNCF and RuO₂/PNCF electrodes

A total of 50 mg of Pt/C or RuO₂ powder was dispersed into a 5 mL mixture of ethanol containing 100 μL of Nafion solution (5 wt%) by ultrasonication for 30 min. Then, 1850 μL of powder ink was loaded onto the PNCF surface (electrode surface area: 1 × 1 cm²) and dried at room temperature for later testing.

2.6 | Materials' characterization

The structures of the obtained samples were analyzed using a field-emission scanning electron microscope (SEM, JSM-6700F) and a transmission electron microscope (TEM, JSM2100), both manufactured by JEOL, Japan. The crystalline structure and elemental states of the samples were analyzed using an X-ray diffractometer

(Thermo Fisher Scientific; XRD) and X-ray photoelectron spectroscopy (XPS). The K α XPS instrument was manufactured by Thermo Scientific, with the Al K α (1486.6 eV) X-ray source set at 300 W. The thickness of the N-YNiCoP nanosheet was estimated using atomic force microscopy (AFM) on a instrument (XE-100E). To prevent unwanted sample damage, Raman spectroscopy was carried using a 532 nm line excited by a 50 mW laser; and an objective lens of 8 mm with 50 times magnification. X-ray absorption spectroscopy (XAS) was performed at the Australian Synchrotron (XAS beamline) utilizing Si(111) crystals cooled in liquid nitrogen. Meanwhile, the energy of the electron beam was set to 3.0 GeV. Assisted by the integrated beamline optics (Si-coated collimating and Rh-coated focusing mirrors), higher harmonics of the incident X-ray beam were minimized. A specialized Ge 100 element detector was used to acquire a fluorescent signal; the energy was calibrated utilizing a Y (Co, Ni) foil. The size of the incident beam was about $1 \times 1 \text{ mm}^2$, and it took about an hour to record a single XAS spectrum.

2.7 | Electrochemical measurements

The electrochemical measurements were performed using a standard electrochemical workstation (CHI 660E; Shanghai Chenhua Instr. Co.) in a 1.0 M KOH solution (at pH 14°C and 25°C). To obtain a consistent result, all tests were performed without gas pretreatment for the alkaline medium, similar to previous work.¹⁸ The testing was carried using a three-electrode system. In this system, the sample is used as the working electrode, a carbon rod is used as the counter-electrode, and Hg/HgO acts as the reference electrode. The electrochemical data are modified with respect to the reversible hydrogen electrode (RHE), following $E_{\text{vsRHE}} = E_{\text{vsHg/HgO}} + 0.095 + 0.059 \text{ pH}$ (Nernst equation). Based on the equation: $E_{\text{Corrected}} = E_{\text{Raw}} - 95\% iR_s$, the polarization curves are iR -corrected (95%), taking into account the solution's Ohmic resistance. It is noteworthy that the samples were cut into $0.5 \times 0.5 \text{ cm}^2$ pieces and placed in a 1.0 M KOH solution as working electrodes. These working electrodes were activated using cyclic voltammetry (CV) operated at a 5 mV s^{-1} sweep rate, while linear sweep voltammetry (LSV) was carried at a 1 mV s^{-1} scanning rate. Electrochemical impedance spectroscopy was performed within the frequency range of 0.02 Hz–100 kHz, with the AC voltage amplitude (5 mV) at different potentials. Meanwhile, the C_{dl} (double-layer capacitance) value was used to estimate electrochemical active surface area (ECSA). ECSA was calculated based on the CV curves recorded

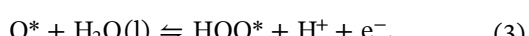
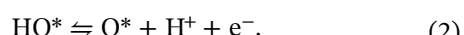
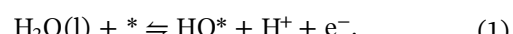
from -0.6 to -0.4 V at scanning rates of 20, 60, 100, 140, 180, and 200 mV s^{-1} . Moreover, the turnover frequency (TOF) values for both HER and OER reactions were quantified as $\text{TOF}_{\text{HER}} = jS/2nF$ and $\text{TOF}_{\text{OER}} = jS/4nF$.¹⁰ Here, S is the electrode surface area, j is the current density, F ($96,485 \text{ C mol}^{-1}$) is the Faradaic constant, and n (mol) represents the quantity of the active substance. For a comparison, the HER and OER performances of PNCF coated with Pt/C and RuO₂ powder under the same loading parameters as N-YNiCoP (18.5 mg cm^{-2}) were also tested.

2.8 | DFT calculations

Modeling of structural relaxation and electronic energy was carried by using spin-polarized DFT, incorporated into the Vienna Ab initio Simulation Package simulation package. During the simulations, the projector augmented-wave model was used, where 400 eV was the cut-off value for the plane-wave energy. The Perdew–Burke–Ernzerhof functional was used to quantify the relevant correlation–exchange energies. Sampling across the Brillouin zone was carried using the $2 \times 2 \times 1$ Monkhorst–Pack grid. To eliminate the interference of periodic structures, a 20 \AA vacuum layer was added. To calculate the energy of adsorption and quantify van der Waals (vdW) interactions, the vdW-DF3 correlation was applied.¹⁹ The standard optimization of geometry was repeatedly carried out to eventually achieve a low total energy tolerance below $1 \times 10^{-5} \text{ eV}$; the corresponding changes of the atomic forces appeared to be below $10^{-4} \text{ eV \AA}^{-1}$.

In addition, to assess the HER and OER activity of the atomistic models, the Gibbs free energy of the elementary coordinate steps and the HER and OER overpotentials were calculated. The calculation method follows the previously published method.^{3,20}

To quantify the catalyst activity in OER, the Gibbs free energy and overpotential for each reaction step were calculated following the four-electron mechanism²⁰:



In Reactions (1–4) above, asterisks (*) represent catalytically active sites, whereas labels (l) and (g) denote the liquid and gas phases, respectively.

3 | RESULTS AND DISCUSSION

3.1 | Fabrication and characterization

As shown in Figures 1A and S1, the cleaned NCF surface is modified by the DBD plasma to create dense microtrenches,²¹ which exposes a higher density of Ni and Co atoms for the subsequent hydrothermal reactions. Importantly, NiCo LDH is successfully formed on the PNCF surface after a hydrothermal process when the Y³⁺ ions are present in the reactive reagent, which cannot be obtained without adding Y³⁺ ions under the same reaction conditions. The possible reason for this phenomenon may be that the electron clouds of Co and Ni atoms are adversely affected by the strong electronegativity of Y³⁺ ions, and the positive ends of Ni and Co atoms may more easily combine with hydroxide ions for the synthesis of YNiCo LDH. Furthermore, the self-supported YNiCo LDH precursor is successfully transformed into N-doped NiCoP structures by the nitrogen plasma-assisted phosphating process. According to our previous work,^{10,14} the hydrothermal and phosphating conditions have a fundamental effect on the structure of the catalyst intermediate and the electrocatalytic performance of the targeted electrocatalyst. When the process temperature is too low or the reaction time is too short to enable the engineering of transition-metal LDH intermediates, the catalyst distribution is sparse and inhomogeneous, which reduces the catalytic activity. On the contrary, excessive crystallinity or aggregation of the catalyst reduces proton transport rates. To synthesize the optimized YNiCo LDH, as shown in Figures S2–S4, the HER and OER performances of YNiCo LDH/PNCF engineered with different experimental parameters are explored, and the optimized YNiCo LDH/PNCF (mass of Y: 0.06 g, temperature of the reaction: 180°C, time of reaction: 10 h) has the smallest electrocatalytic resistance and presents the best performance for the overall water splitting. The influence of the parameters of plasma-assisted phosphating is investigated as well. As can be seen in Figures S5–S8, the best catalyst structure can be prepared when the mass of red P, phosphating temperature, reaction time, and RF power are 0.2 g, 550°C, 2 h, and 100 W, respectively.

Figure 1B shows the high-resolution SEM micrograph of inter-crosslinked ultrathin YNiCo LDH, and the nanosheets are uniformly sprouted from the frame of the NiCo alloy foam (inset), which enables maintenance of long-term electrocatalytic stability.²⁰ Meanwhile, the dense voids created by connected nanosheets can possibly aid in gas desorption and electron/proton transport, leading to higher HER and OER activity. According to previous work,¹⁰ NiCo alloy foam as the

reactive source of Ni and Co elements cannot yield any nanosheets under similar process conditions as growing YNiCo LDH, unless higher temperatures and longer reaction times are used. Therefore, the high electronegativity (EN: 14.82) of rare-earth Y³⁺ ions is crucial for inducing YNiCo LDH *in situ* under moderate reaction conditions. To verify this hypothesis, the PNCF was subjected to the same hydrothermal reaction conditions (180°C, 10 h) without adding the Y³⁺ reagent. As shown in Figure S9A, no nanosheets appear on the PNCF surface and only some tetrahedrons of the NiCo compound are formed. Meanwhile, to exclude the carrier effect, the YNiCo LDH sample is fabricated with a Ni/Co powder (in 1:9 ratio, Ni-EN:1.91, Co-EN:1.88) under the same hydrothermal conditions, and the corresponding SEM image in Figure S9B shows that YNiCo LDH nanosheet-like structures are successfully formed. For comparison, we also prepare the NiCo powder sample (Figure S9C) and the Y powder sample (Figure S9D) using the same hydrothermal process parameters, and the results show that the obtained NiCo and Y hydroxides all show particle-like morphology, while the aggregated catalysts cover the reactive sites, which obviously decreases the catalysts' HER and OER activity. Furthermore, YCo and YNi hydroxides are also synthesized on pure Co and Ni foam. As shown in Figures S9E,F, some uneven nanosheets of YCo, similar to the YNiCo LDH precursors in shape, are formed on the Co foam surface, while some floccule/needle-like YNi hydroxides appear on the Ni foam. This phenomenon indicates that Y³⁺ ions and Co atoms play important roles in the *in situ* growth of the YNiCo multiple-phase LDH catalyst. Figure S10 shows the catalytic activities of YNi, YCo, and YNiCo hydroxide for HER and OER, and one can also note that the performance of pure Co foam is better than that of pure Ni foam. However, both these samples show lower performance compared to YNiCo LDH, indicating that trimetallic synergy can effectively enhance the electrocatalytic activity of a multiple-phase catalyst.

To explore nanosheet growth mechanisms, we prepared YNiCo LDH samples using different hydrothermal reaction times. Figure S11A,B shows the SEM images of YNiCo LDH fabricated with reaction times of 15 and 30 min, respectively. Besides, the samples are also analyzed by TEM-energy-dispersive X-ray (EDX) and elemental mapping diagrams. It is noteworthy that many small aggregated YNiCo LDHs are formed on the PNCF surface after 15 min of reaction time, while the cross-linked nanosheets are formed after 30-min reaction, which may be caused by the inner growth strain energy.²² Meanwhile, the elemental concentration of Y increases from 0.03% to 0.05% (Figure S11D,F), and this

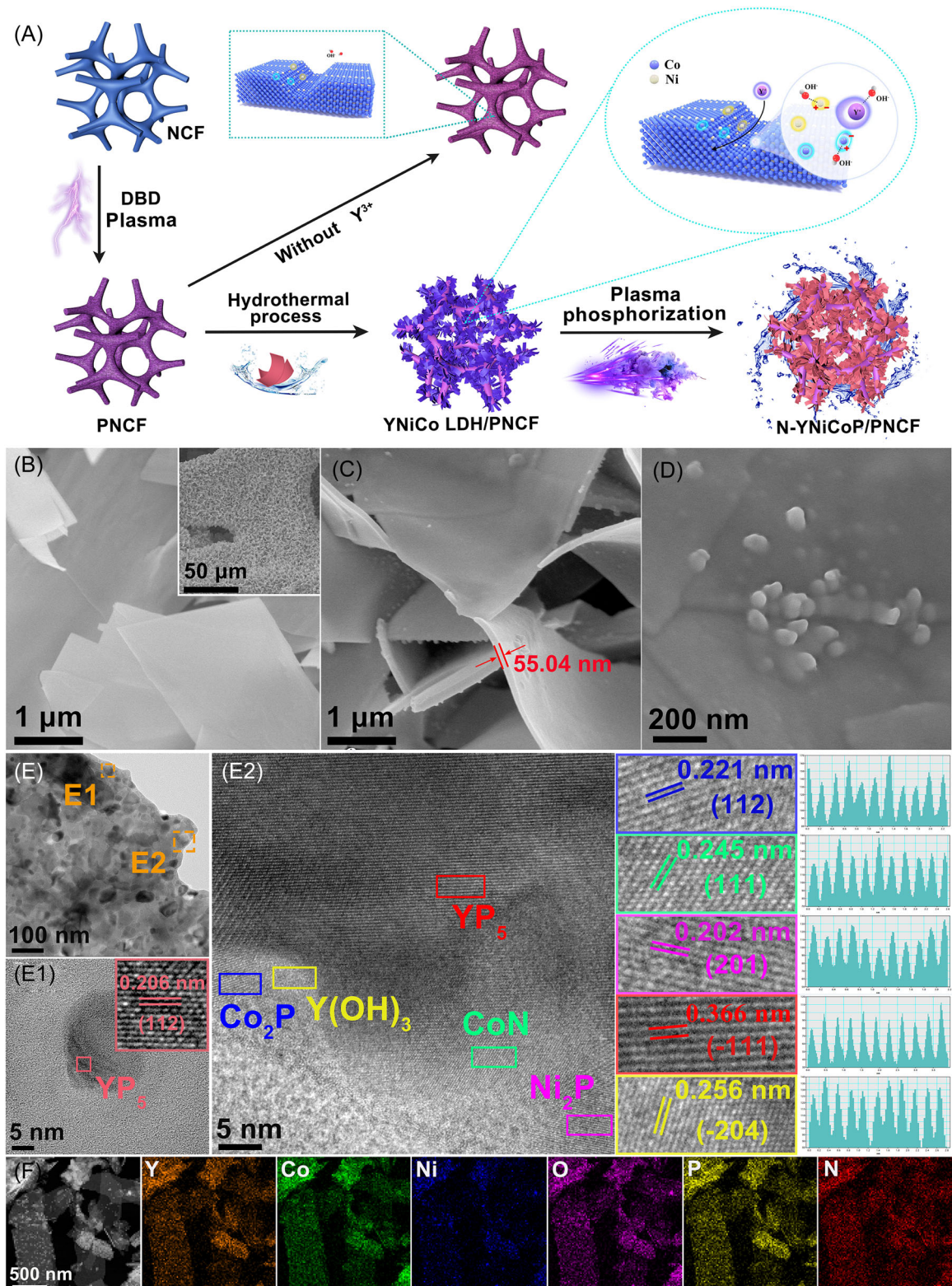


FIGURE 1 (A) Schematic illustrations of the synthesis of N-YNiCoP/PNCF via a three-step process. Physicochemical structures of the synthesized catalysts. SEM images of (B) YNiCo LDH/PNCF and (C, D) N-YNiCoP/PNCF. (E) Low- and (E1–E2) high-resolution TEM images of N-YNiCoP/PNCF and (F) elemental mapping of different atoms detected by TEM.

finding further indicates that the Y ion triggers the formation of NiCo LDH. Noticeably, after 4 h of hydrothermal reaction time, the morphology of the YNiCo nanosheets changes considerably and gradually resembles that of the optimized YNiCo LDH, as shown in Figure S11C. One can thus infer that Y ions first induce the growth of NiCo hydroxide nanosheets and then mix with them to form three-phase YNiCo hydroxides.

Furthermore, the crystal structures of YNiCo LDH/PNCF are investigated by XRD patterns (upper blue line of Figure S12). The peaks are mainly attributed to Y(OH)_3 (JCPDS NO. 21-1447) and Co(OH)_2 (JCPDS NO. 74-1057). Figure S13A shows the high-resolution TEM of YNiCo LDH, and the interplanar spacings of lattice fringes in the center of each crystalline nanosheets are precisely measured to be 0.276 and 0.239 nm, which correspond to the (−211) and (011) planes of Y(OH)_3 and Co(OH)_2 , respectively. Figure S13B shows the low-resolution elemental maps of YNiCo LDH. One can see that the Y, Co, Ni, and O atoms are distributed evenly over the nanosheet surfaces. However, the related crystal phase of Ni cannot be found in the high-resolution TEM image, which is also consistent with the results of XRD. Since many amorphous regions (pink circles) appear on the catalyst nanosheet, one can deduce that Ni atoms are likely present in the amorphous state within the nanosheets; the amorphous phase is likely to make the nanosheets more robust, while inducing charge exchange between the adjacent metal sites to promote water dissociation.²³ To explore the effect of DBD plasma on the HER and OER of YNiCo LDH samples, a control sample without DBD plasma treatment is also synthesized, and the catalytic performance is shown in Figure S14. It can be seen that the HER and OER catalytic activity of YNiCo LDH/PNCF is much higher than that of YNiCo LDH/NCF because the electrocatalytic resistance of YNiCo LDH/PNCF is relatively small. Figure S15A–D shows the effects of the plasma treatment on the YNiCo LDH morphology. Noticeably, many nanosized trenches on the NCF surface can provide larger reactive areas for sprouting YNiCo LDH. As a result, the growth rate of YNiCo LDH on the PNCF is higher than that on the NCF surface, resulting in much better HER and OER performance. Interestingly, although the morphologies of the YNiCo LDH/NCF and YNiCo LDH/PNCF samples are different, according to the XRD results (Figures S16 and S12 upper blue line), the crystal structures are completely consistent. Therefore, the DBD plasma not only promotes the formation of cross-linked three-dimensional nanosheets but also increases electrocatalytic stability because of the stronger connections between YNiCo LDH and PNCF.

Figure 1C shows the morphology of N-doped YNiCoP (N-YNiCoP) fabricated using a plasma-assisted

phosphating method. Compared with the YNiCo LDH precursor, the morphology of N-YNiCoP maintains a similar sheet-like profile, while some nanoparticles are decorated on the smooth surface of N-YNiCoP nanosheets (Figure 1D), which promotes the catalytic stability of N-YNiCoP/PNCF.²⁴ The typical thickness of N-YNiCoP nanosheets is approximately 50–60 nm, which is also confirmed by the AFM images (Figure S17). We emphasize that the optimized thickness of N-YNiCoP nanosheets can ensure excellent electrocatalytic activity and stability in the alkaline medium. Figure S18 shows the elemental map of N-YNiCoP; one can see that Y, Co, Ni, O, P, and N elements are evenly distributed over the nanosheets, which implies that P and N elements are doped into the YNiCo LDH after the plasma-assisted phosphating process. Figure 1E shows the low-resolution TEM image of a N-YNiCoP nanosheet, and some dark nanosized patches are present on the nanosheet plane. Furthermore, the high-resolution TEM micrographs (Figure 1E1,E2) reveal specific lattice planes on the surfaces of the nanosheets. It is noteworthy that the observable dark patches correspond to (112) and (−111) planes of YP_5 , which are characterized by crystal plane spacings of 0.206 and 0.366 nm, respectively. Meanwhile, the other four crystal plane spacings of 0.221, 0.245, 0.202, and 0.256 nm are ascribed to the (112), (111), (201), and (−204) planes of Co_2P , CoN , Ni_2P , and Y(OH)_3 , respectively. Besides, the selected area electron diffraction (SAED) pattern confirms these structural features (Figure S19). Notably, the appearance of the Y(OH)_3 phase may be due to the incompletely phosphated hydroxide nanosheets. Figure 1F shows the distributions of the Y, Co, Ni, O, P, and N elements over the N-YNiCoP nanosheets, which confirms that the trimetallic N-YNiCoP is successfully formed on the PNCF by the hybrid hydrothermal and plasma-assisted phosphating process.

Furthermore, the crystal structures of N-YNiCoP/PNCF are also investigated by XRD diffractometry. As can be seen in Figure S12, the XRD peaks at 24.24°, 26.56°, 27.84°, 42.30°, 43.99°, 61.94°, and 61.95° are indexed to the (−111), (120), (101), (220), (112), (−223), and (−312) planes, respectively, of the monoclinic phases of YP_5 crystals (JCPDS 86-2182). In addition, the peaks at 40.72°, 40.98°, and 51.54° are attributed to the (112), (210), and (113) planes of the orthorhombic phases of Co_2P (JCPDS 89-3030), respectively. The XRD peaks appearing at 40.71°, 44.61°, and 47.36° are attributed to (111), (201), and (210) planes of the hexagonal phases of Ni_2P (JCPDS NO. 89-2742), respectively. It is noteworthy that the diffraction peak at 36.19° is attributed to the (111) cubic plane of CoN (JCPDS NO 16-0116), and the above results indicate that N-doped heterogeneous

phosphides are successfully synthesized. Meanwhile, the chemical structure and elemental composition of the N-YNiCoP are investigated using XPS (Figure S20 and Table S1). Compared with the atoms exposed in YNiCo LDH, the main spin states of Y 3d, Co 2p, Ni 2p, and O 1s in N-YNiCoP change slightly. However, new chemical states arise after doping with P (14.72%) and N (2.57%) atoms. Therefore, the formed multiple chemical phases and heterointerfaces may promote high HER and OER performance. It is noteworthy that the C element is possibly introduced during the NCF synthesis, while the O element may arise from untransformed YNiCo LDH or adsorbed oxygen on the catalyst surface.⁹ The elemental chemical states of N-YNiCoP are also investigated by XPS spectroscopy. As shown in Figure S20, the Y 3d (Y⁵⁺ and Y³⁺), Co 2p (Co²⁺ and Co³⁺), Ni 2p (Ni²⁺ and Ni³⁺), O 1s (O-H and O-P), P 2p (M-P), and N 1s (Co-N and N-O) states appear in the high-resolution XPS spectra of N-YNiCoP.^{10,14,25,26} The diverse ionic states within the catalyst are very useful for optimizing the charge exchange and electron transport, resulting in high electrolysis performance. Specifically, nitrogen atoms are successfully incorporated into YNiCoP during the PECVD process. It is noteworthy that N 1s peaks seen at 400.02 and 402.04 eV can be attributed to Co-N and N-O bonds, respectively. These bonds are vital for accelerating the catalytic activity of the in situ-engineered N-YNiCoP/PNCF catalysts. Related studies have shown that the introduction of a N element can modulate electronic states in the atoms located in the reactive sites. For instance, the electrons may occupy higher energy levels (close to the Fermi level), which effectively enhances the charge transfer across the active interface.^{27,28}

To investigate the effect of Y on the catalyst, we prepare a nanosheet sample (N-NiCoP/PNCF) without adding Y, and further investigate the electronic states of N-NiCoP and N-YNiCoP samples by X-ray absorption near-edge structure (XANES) and extended X-ray absorption fine structure absorption spectroscopy (EX-AFS). Figure 2A shows the XANES of Co K-edge spectra, which show that the pre-edge peaks of the N-NiCoP and N-YNiCoP samples are between the peaks for the Co foil and CoO, indicating that their valence states are between 0 and +2. Furthermore, as shown in Figure S21A, by using the energy of metal Co as the original point and utilizing an area integration method, the average Co valence in N-NiCoP is +0.96, and this value is then increased to +1.43 for N-YNiCoP. The EXAFS spectra of Co in the K-space in Figure S21B suggest that the measured data have a relatively small signal-noise ratio, indicating good data quality. To investigate the local atomic coordination environments, Fourier-transform extended X-ray absorption fine structure spectroscopy

(FT-EXAFS) is performed (Figure 2B). One can note that the peaks at ~2.09 Å are attributed to the Co-P scattering path for N-YNiCoP and N-NiCoP, which is different from the Co-Co and Co-O scattering paths in the Co foil or CoO.^{19,29} Furthermore, when the Y element is mixed into the multiple-phase metal phosphide, the peak position of Co-P bonds slightly decreases (Figure 2B), and this observation indicates that the Co-P bond length is shortened, which will cause stronger bonding intensity and improve the catalyst's stability. Compared with N-NiCoP, as shown in Figure S21C, the Co-P peak intensity of N-YNiCoP is also slightly lower, indicating that the incorporation of Y helps reduce the coordination number of the first shell of Co ions. Normally, the lower coordination number indicates that N-YNiCoP has a smaller central-ion radius, while the interatomic bonding is stronger, which also means that Y incorporation helps improve the structural stability of N-YNiCoP. As shown in Figure S22, compared to N-NiCoP/PNCF, N-YNiCoP/PNCF shows significantly enhanced electrocatalytic stability for the HER process, thereby further substantiating this conclusion. Meanwhile, the peak at 1.35 Å is attributed to the Co-N scattering path (Figure S21C), consistent with the results of TEM and XRD analyses. Figure 2C shows the wavelet transform (WT) corresponding to the EXAFS spectra, and the optimized Co K-edge WT-EXAFS for the Co-P oscillation of N-YNiCoP has the maximum intensity at 5.92 Å⁻¹, which is close to that of N-NiCoP (6.04 Å⁻¹). However, it is distinct from the intensities of Co-O oscillation of CoO (5.3 Å⁻¹) and the Co-Co oscillation of both the Co foil (7.96 Å⁻¹) and CoO (7.32 Å⁻¹).³⁰ Similarly, XANES of Ni K-edge spectra is also obtained. As shown in Figure 2D, the average valences of Ni for N-NiCoP and N-YNiCoP are calculated to be +1.66 and +1.23 (Figure S21D), respectively.³¹ Meanwhile, EXAFS of Ni in the K-space is shown in Figure S21E, which also indicates that high-quality X-ray absorption data are obtained. Figure 2E shows FT-EXAFS in the R-space, and the peaks at ~2.06 Å are attributed to the Ni-P scattering path for N-YNiCoP and N-NiCoP, which is different from the Ni-Ni and Ni-O scattering paths in the Ni foil or NiO.^{32,33} Furthermore, similar to the Co results, the addition of Y decreases the coordination number around the Ni atom, as also demonstrated by resulting WT-EXAFS of Ni (Figure 2F). In addition, to resolve the chemical microenvironment of the catalyst after embedding a Y atom, the XANES, EXAFS, and FT-EXAFS spectra are also examined. As shown in Figure 2G, the Y curve of N-YNiCoP shifts toward a higher energy state, and Y is present as a cation rather than as a neutral atom, which suggests that Y forms a polyphasic compound with NiCo. Besides, as shown in Figure S23A,B, the peak at 2.58 Å is

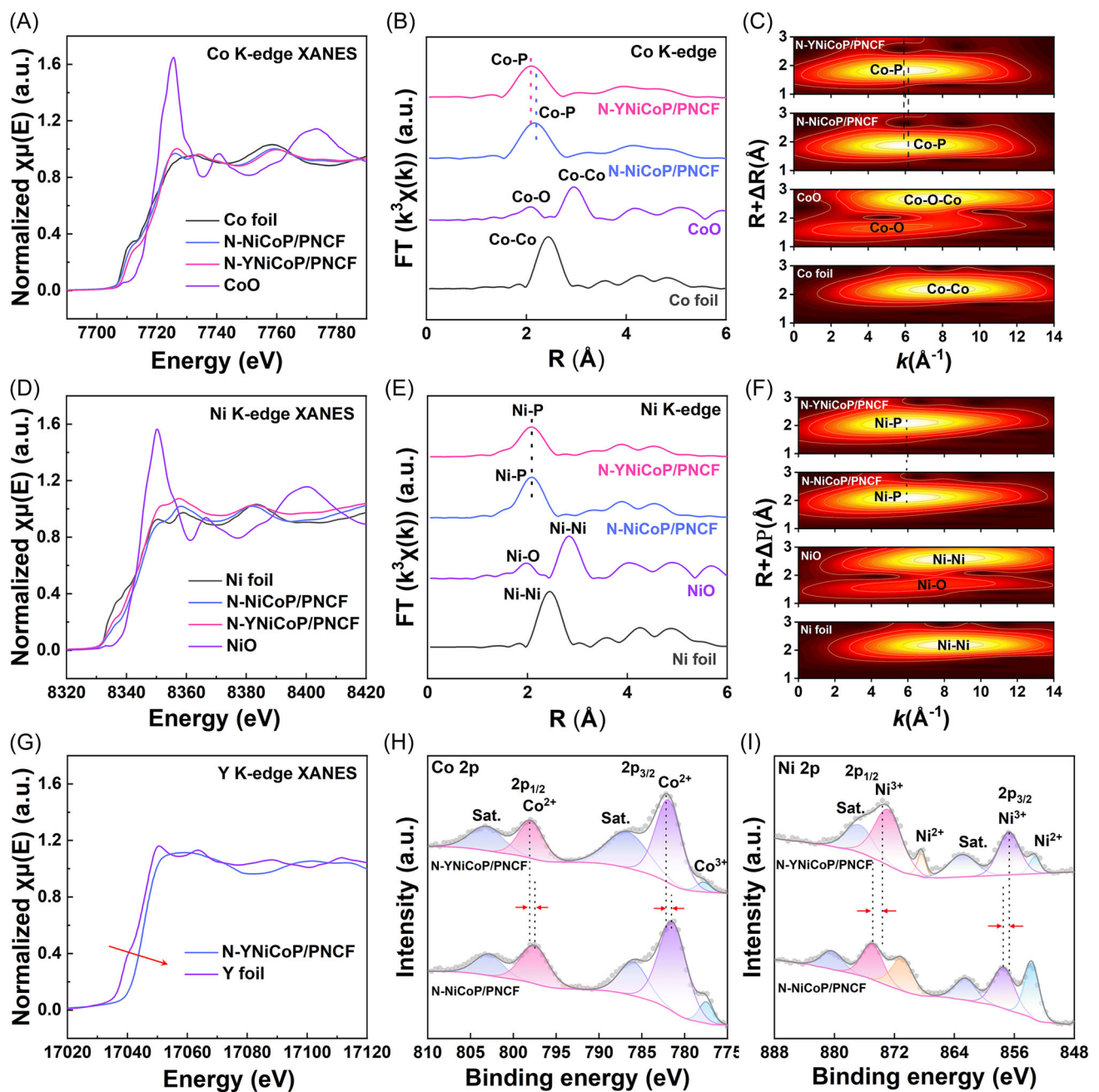


FIGURE 2 Surface structure of N-YNiCoP/PNCF and reference samples investigations by XAS. (A) Co K-edge XANES, (B) Co K-edge FT-EXAFS spectra, (C) Co K-edge WT-EXAFS spectra, (D) Ni K-edge XANES, (E) Ni K-edge FT-EXAFS spectra, (F) Ni K-edge WT-EXAFS spectra, and (G) Y K-edge XANES. XPS spectra of (H) Co 2p and (I) Ni 2p of N-YNiCoP/PNCF and N-NiCoP/PNCF samples.

attributed to the Y-P or Y-O scattering path for N-YNiCoP or Y(OH)_3 ,³⁴ which is different from the Y-Y scattering path in the Y foil.³⁵ Figure 2H,I shows the high-resolution Co 2p and Ni 2p XPS spectra of N-YNiCoP and N-NiCoP. When Y is added, the Co and Ni peaks shift to high and low energy levels, respectively, consistent with the results of XAS spectroscopy. Collectively, the above results indicate that the addition of the Y element significantly changes the electronic structure and coordination environment of Ni and Co, which will

effectively tune the catalytic activity and stability of the produced electrocatalyst.

3.2 | HER performance

Figure 3A shows the polarization curves (LSV) of the NCF, NiCo LDH/PNCF, YNiCo LDH/PNCF, YNiCoP/PNCF, N-YNiCoP/PNCF, and Pt/C/PNCF catalysts in 1 M KOH electrolyte after an iR -correction. To compare

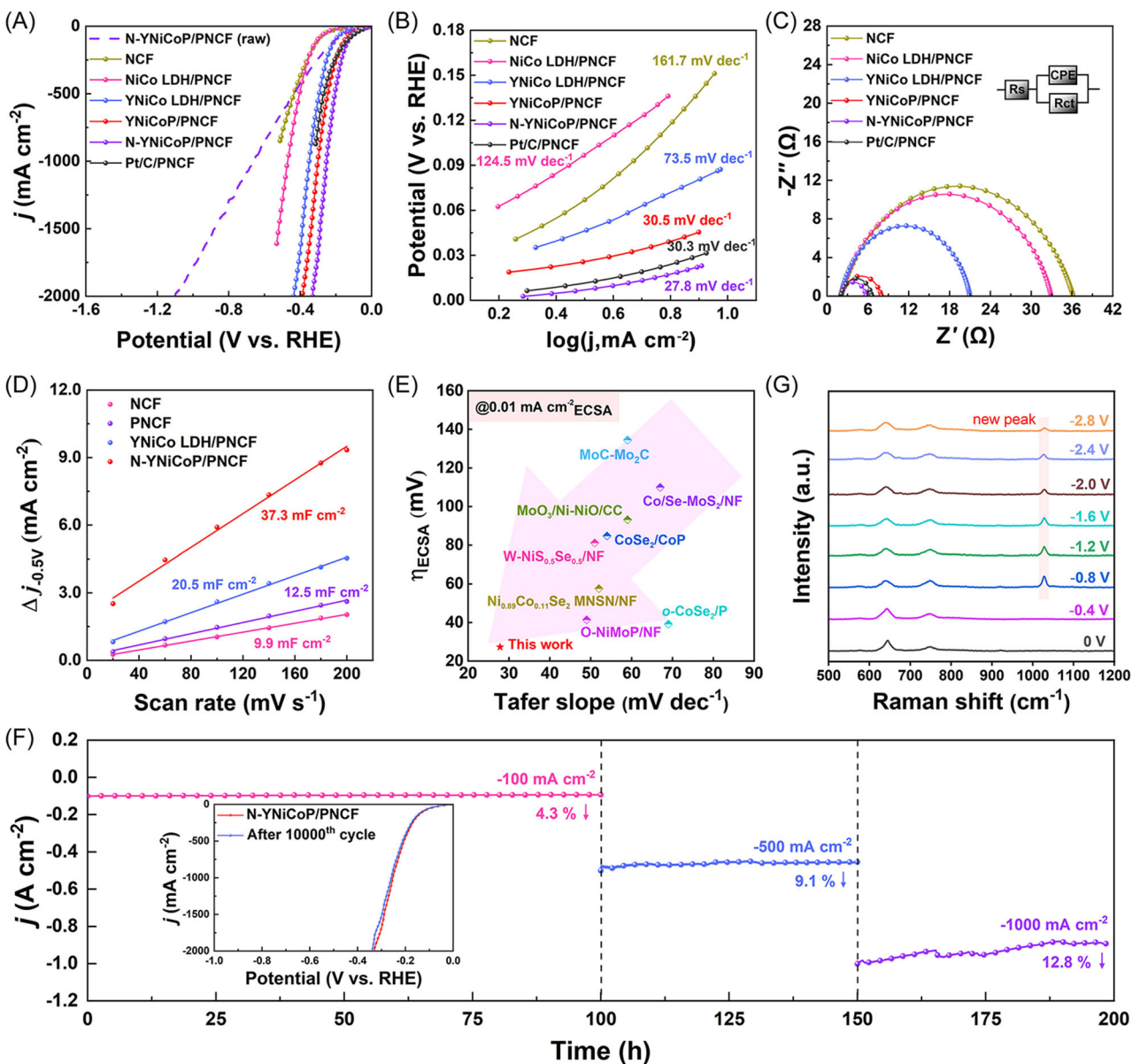


FIGURE 3 HER performance of different catalysts in 1.0 M KOH electrolyte. (A) Polarization curves, (B) Tafel slopes, (C) Nyquist plots, (D) C_{dl} curves, (E) comparison of the overpotentials and Tafel slope at 0.01 mA cm⁻² normalized by ECSA with other state-of-the-art electrocatalysts, (F) chronoamperometric curves of N-YNiCoP/PNCF recorded at j_{100} , j_{500} , and j_{1000} for 200 h and polarization curves of N-YNiCoP/PNCF before and after 10,000 cycles (inset), and (G) in situ Raman spectra of N-YNiCoP/PNCF (from 0 to -2.8 V) in 1 M KOH.

the HER performance of the obtained catalysts, the exact overpotential results corresponding to different current densities are listed in Table S2. Notably, YNiCo LDH/PNCF (blue line) shows higher HER activity than NiCo LDH/PNCF (pink line), because the Y³⁺-induced nanosheet structure significantly increases the catalytic active area and improves the proton transport efficiency. Due to the N-doping, which obviously decreases the Gibbs energy for absorbing H ions,¹⁰ the catalytic performance of N-YNiCoP/PNCF (purple line) is clearly

better than that of YNiCoP/PNCF (red line). Furthermore, to operate under high current density conditions (1000 and 2000 mA cm⁻²) expected for commercial applications, the N-YNiCoP/PNCF catalyst requires low overpotentials of 252 (j_{1000}) and 331 (j_{2000}) mV, respectively. The Tafel slope is commonly used to quantify the intrinsic reaction kinetics of the engineered catalysts.³⁶ Normally, three distinctive steps of reactive kinetics are involved in the HER process, namely, Tafel (≤ 30 mV dec⁻¹), Heyrovsky (40–120 mV dec⁻¹), and Volmer

($\geq 120 \text{ mV dec}^{-1}$).^{19,36} As can be seen in Figure 3B, the Tafel slope of N-YNiCoP/PNCF (27.8 mV dec^{-1}) is much lower than that of YNiCoP/PNCF (30.5 mV dec^{-1}). The results indicate that the N-YNiCoP/PNCF catalyst has fast H₂ generation kinetics and corresponds to a Tafel scenario (lower than 30 mV dec^{-1}). Figure 3C shows the electrochemical impedance of the engineered catalysts, which is also an important factor for studying the HER kinetics.³ The interface charge-transfer resistance (R_{ct}) of N-YNiCoP/PNCF is only 3.3Ω , which is much smaller than that of YNiCoP/PNCF (5.9Ω), indicating that N-YNiCoP/PNCF has higher rates of electron transfer. Therefore, the Y³⁺-induced and N-doped unique physicochemical structure of N-YNiCoP/PNCF can significantly improve the electrocatalytic activity for H₂ evolution.

The values of C_{dl} (electrochemical double-layer capacitance) and ECSA (C_{dl}/C_s , where $C_s = 0.04 \text{ mF cm}_{\text{geo}}^{-2}$) are commonly used to characterize electrocatalytic activity.²¹ Thanks to the nonsmooth surface of the ultrathin nanosheets, which effectively increases the catalytically active area, as shown in Figures 3D and S24, the calculated values of C_{dl}/ECSA of N-YNiCoP/PNCF ($37.3 \text{ mF cm}^{-2}/932.5 \text{ cm}^{-2}$) are much higher than those of YNiCo LDH/PNCF ($20.5 \text{ mF cm}^{-2}/512.5 \text{ cm}^{-2}$), PNCF ($12.5 \text{ mF cm}^{-2}/312.5 \text{ cm}^{-2}$), and NCF ($9.9 \text{ mF cm}^{-2}/247.5 \text{ cm}^{-2}$) samples. Therefore, the N-YNiCoP/PNCF structure provides greater contact area between the catalyst and the electrolyte, thereby improving electron transfer and catalytic activity. At the same time, N-YNiCoP/PNCF only requires 27.3 mV to generate 0.01 mA cm^{-2} _{ECSA}, which is better than those reported for recently reported alkaline catalysts (Figure 3E), such as O-NiMoP/NF (49 mV dec^{-1} and 41.4 mV),⁸ o-CoSe₂/P (69 mV dec^{-1} and 39.2 mV),²⁶ Ni_{0.89}Co_{0.11}Se₂ MNSN/NF (52 mV dec^{-1} and 57.6 mV),³⁶ W-NiS_{0.5}Se_{0.5}/NF (51 mV dec^{-1} and 81.2 mV),¹ CoSe₂/CoP (54 mV dec^{-1} and 84.8 mV),¹⁷ MoO₃/Ni-NiO/CC (59 mV dec^{-1} and 93.2 mV),³⁷ Co/Se-MoS₂/NF (67 mV dec^{-1} and 110 mV),³⁸ and MoC-Mo₂C (59 mV dec^{-1} , 134.5 mV).³⁹ To confirm this conclusion, the values for the above catalyst activity are normalized by ECSA (Figure S25), and reliable comparison results are achieved.

Normally, TOF is a crucial characteristic for electrocatalytic activity.²¹ As shown in Figure S26A and Table S3, the TOF at 200 mV for N-YNiCoP/PNCF is 9.39 s^{-1} , which is superior to those of YNiCo LDH/PNCF (1.97 s^{-1}) and Pt/C/PNCF (5.66 s^{-1}). In addition, the mass activity (MA) of the synthesized catalysts is also studied (Figure S26B and Table S4), and the MA values of N-YNiCoP/PNCF, YNiCo LDH/PNCF, and Pt/C/PNCF samples under a 200 mV overpotential are 22.65 , 5.58 , and 12.44 A g^{-1} , respectively. Therefore, the high TOF and MA values of N-YNiCoP/PNCF indicate that higher

intrinsic HER activity is achieved. As shown in Table S5, even when compared to recently reported advanced catalysts, N-YNiCoP/PNCF still shows superior TOF and MA values, indicating that N-YNiCoP/PNCF has higher intrinsic catalytic activity for the HER process. Meanwhile, the measured H₂ production rate of N-YNiCoP/PNCF with j_{10} is 2.27 mmol h^{-1} (Figure S27), which is superior to those of recently reported catalysts, such as NiTe-NiSe/NFF (2.07 mmol h^{-1}),³ N-NiVFeP/NFF (1.61 mmol h^{-1}),⁹ Ni₁₂P₅-Fe₂P-NbP/PNF (1.49 mmol h^{-1}),²¹ CoNiSe₂@CoNi-LDHs/NF (0.98 mmol h^{-1}),² W-NiS_{0.5}Se_{0.5}/NF (0.23 mmol h^{-1}),¹ and NiS_{0.5}Se_{0.5} (0.19 mmol h^{-1}).¹ Figure 3F shows the results of long-term stability tests of the N-YNiCoP/PNCF catalyst performed at different constant current densities in 1 M KOH . It is noteworthy that the current density-time characteristic remains stable at j_{100} , decreasing by only 4.3% over 100 h . Meanwhile, N-YNiCoP/PNCF also maintains excellent electrocatalytic stability under high current densities of j_{500} or j_{1000} , which only decreases by 9.1% or 12.8% , respectively. Besides, the excellent electrochemical stability of the N-YNiCoP/PNCF catalyst is further confirmed by the LSV curves before and after 10,000 cycles. The comparison shows that the measured polarization curves are almost the same (inset of Figure 3F).

To study the influence of electrolysis on the catalyst, a series of tests was conducted to investigate the physicochemical structure of N-YNiCoP/PNCF undergoing a 200-h current-time test. Figure S28A,B shows the SEM images under different magnifications, and one can see that the surface morphology of N-YNiCoP changes only slightly after the long-term HER measurements, while the nanosheet structure is still preserved; this may be one of the reasons for the long-term electrocatalytic stability of the catalyst that is achieved. Figure S28C,D shows the TEM images of the N-YNiCoP nanosheet after the HER operation, and the plane spacings of 0.332 , 0.219 , 0.202 , and 0.251 nm are attributed to the (120), (112), (201), and (111) planes of YP₅, Co₂P, Ni₂P, and CoN, respectively, while the SAED patterns also confirm the existence of these constituent substances (Figure S28E). Figure S28F shows the results of the low-resolution elemental mapping, and the Y, Co, Ni, O, P, and N atoms are evenly distributed across the nanosheet surfaces. It is worth noting that the content of Y and P elements decreases compared to the pristine samples. TEM-EDX (Figure S29B) and XPS (Table S1) data also confirm this conclusion, indicating that some Y and P atoms on the N-YNiCoP/PNCF surface are consumed during the HER process, which may be responsible for the slightly decreased performance after the long-time operation. Interestingly, although the surface morphology of N-YNiCoP changed slightly, one can see from the XRD

pattern (Figure S30) that the crystal phase structure is hardly changed compared with the initial structure. It should be noted that the chemical states of some elements (e.g., Y and Ni) exposed on the N-YNiCoP surface disappeared after long-term HER testing (Figure S31). The observed phenomenon indicates that the main framework of N-YNiCoP is highly stable, but the physicochemical structure of the catalyst surface is changed obviously under harsh conditions of long-term HER. Thus, the reason why the N-YNiCoP/PNCF catalyst shows excellent electrocatalytic activity and stability of HER for 200 h in the alkaline electrolyte may be attributed to the multiphase self-supporting heterostructure and the synergistic interaction between the three metallic compounds within the catalyst, and the effect of consumed Y and Ni compounds, which are exposed on the catalyst surface, can be neglected.

Furthermore, *in situ* Raman spectroscopy is used to monitor the structural evolution of the catalyst surface in the HER process (Figures 3G and S32). As expected, the peaks at 645 and 741 cm⁻¹ are caused by extending and flexing vibrational modes of the functional group of the Co–O and NiO bonds, respectively. It is noteworthy that a peak appears at 1028 cm⁻¹ when -0.8 V voltage is applied, which can be attributed to the A_{1g} mode of Ni–O.^{40–42} This result indicates that the metal–oxygen configuration, as a reaction intermediate, not only promotes the structural stability but also fully exposes the surface active sites and improves the reactive kinetics.^{30,43} However, with increasing voltage, the peak intensity gradually decreases, which can be attributed to the fact that the generation of many bubbles in the electrolytic process affects the laser penetration and focus.

3.3 | OER performance

The OER performance of N-YNiCoP/PNCF in 1 M KOH is also evaluated by *iR*-correction. As can be seen in Figure 4A and Table S6, N-YNiCoP/PNCF shows excellent OER activity based on the fact that the overpotentials for delivering j_{100} , j_{500} , j_{1000} , and j_{2000} are only 316, 379, 412, and 464 mV, respectively, which is better than that of YNiCoP/PNCF (329 mV/ j_{100} , 402 mV/ j_{500} , 412 mV/ j_{1000} , and 464 mV/ j_{2000} , respectively), as well as much higher than that of NiCo LDH/PNCF. The above results prove that the incorporation of both Y and N atoms promotes an increase in the OER performance of the engineered catalysts. Notably, a similar HER variation trend is also seen, and the OER activity gradually exceeds the activity of the noble-metal-based catalyst (RuO₂/PNCF) at current densities above the critical

value. Figure 4B shows the calculated Tafel slope of N-YNiCoP/PNCF (62.8 mV dec⁻¹), which is much lower than those of YNiCoP/PNCF (98.4 mV dec⁻¹), YNiCo LDH/PNCF (87.8 mV dec⁻¹), NiCo LDH/PNCF (106.5 mV dec⁻¹), NCF (110.2 mV dec⁻¹), and RuO₂/PNCF (71.3 mV dec⁻¹), indicating that the optimized catalyst has faster OER reaction kinetics. The corresponding Nyquist plots of the synthesized electrocatalysts are shown in Figure 4C, and R_{ct} (interface charge-transfer resistance) of N-YNiCoP/PNCF (1.5 Ω) is lower than those of YNiCoP/PNCF (1.9 Ω), YNiCo LDH/PNCF (6.9 Ω), NiCo LDH/PNCF (12.2 Ω), and NCF (15.4 Ω), and close to that of RuO₂/PNCF (1.3 Ω), indicating that N-YNiCoP/PNCF has higher electron transfer rates and higher activity in OER. Furthermore, all LSV characteristics of the resulting catalysts are normalized on the ECSA value (Figure S33A), and it can be seen that N-YNiCoP/PNCF still has the highest catalytic activity for OER. As shown in Figure S33B, N-YNiCoP/PNCF only needs 171 mV to induce 0.01 mA cm⁻² ECSA, which is superior to the reported catalysts, such as CoMoNiS/NF (58 mV dec⁻¹ and 195 mV),⁴⁴ NiTe-NiS/NF (49 mV dec⁻¹ and 201 mV),⁴⁵ N-NiVFeP/NFF (72 mV dec⁻¹ and 212 mV),⁹ NiTe₂/Ni(OH)₂/CFC (75 mV dec⁻¹ and 221 mV),⁴⁶ NiCoP@NC NA/NF (70.5 mV dec⁻¹ and 245 mV),⁴⁷ Cu₃Se₂@CoSe₂-NiSe₂/PNCF (87 mV dec⁻¹ and 261 mV),⁴⁸ two-tiered NiSe/NF (77.1 mV dec⁻¹ and 282 mV),⁴⁹ and N-NiCoP_x/NCF (61 mV dec⁻¹ and 286 mV).¹⁰

Likewise, the values of TOF and MA were also determined to evaluate the electrocatalytic activity. As presented in Tables S7 and S8, the values of TOF and MA of N-YNiCoP/PNCF gradually exceed those of YNiCo LDH/PNCF and RuO₂/PNCF when the voltage is increased beyond the critical value. It is noteworthy that N-YNiCoP/PNCF still shows high TOF and MA values even compared to recently reported high-quality catalysts (Table S9). These results further reveal that N-YNiCoP/PNCF has remarkable catalytic activity for O₂ evolution. Figure S34 shows that the amount of O₂ generated by N-YNiCoP/PNCF with j_{10} (0.98 mmol h⁻¹) is better than those of recently reported high-performance catalysts, including NiTe-NiSe/NFF (0.9 mmol h⁻¹),³ W-NiS_{0.5}Se_{0.5}/NF (0.89 mmol h⁻¹),¹ N-NiVFeP/NFF (0.81 mmol h⁻¹),⁹ Ni₁₂P₅-Fe₂P-NbP/PNF (0.71 mmol h⁻¹),²¹ CoNiSe₂@CoNi-LDHs/NF (0.45 mmol h⁻¹),² and NiS_{0.5}Se_{0.5} (0.1 mmol h⁻¹).¹ Besides, the Faradaic efficiency of N-YNiCoP/PNCF is close to 100% because the production amount of O₂ is almost half that of H₂, thus approaching the theoretical value of 1/2. Importantly, N-YNiCoP/PNCF can maintain a long-term high-current operation (Figure 4F), which is confirmed by the stable current density-time curves at j_{10} , j_{100} , and j_{200} under harsh alkaline conditions (pH 14). Similarly, almost identical LSV curves recorded before (blue) and after (red) the 10,000 CV

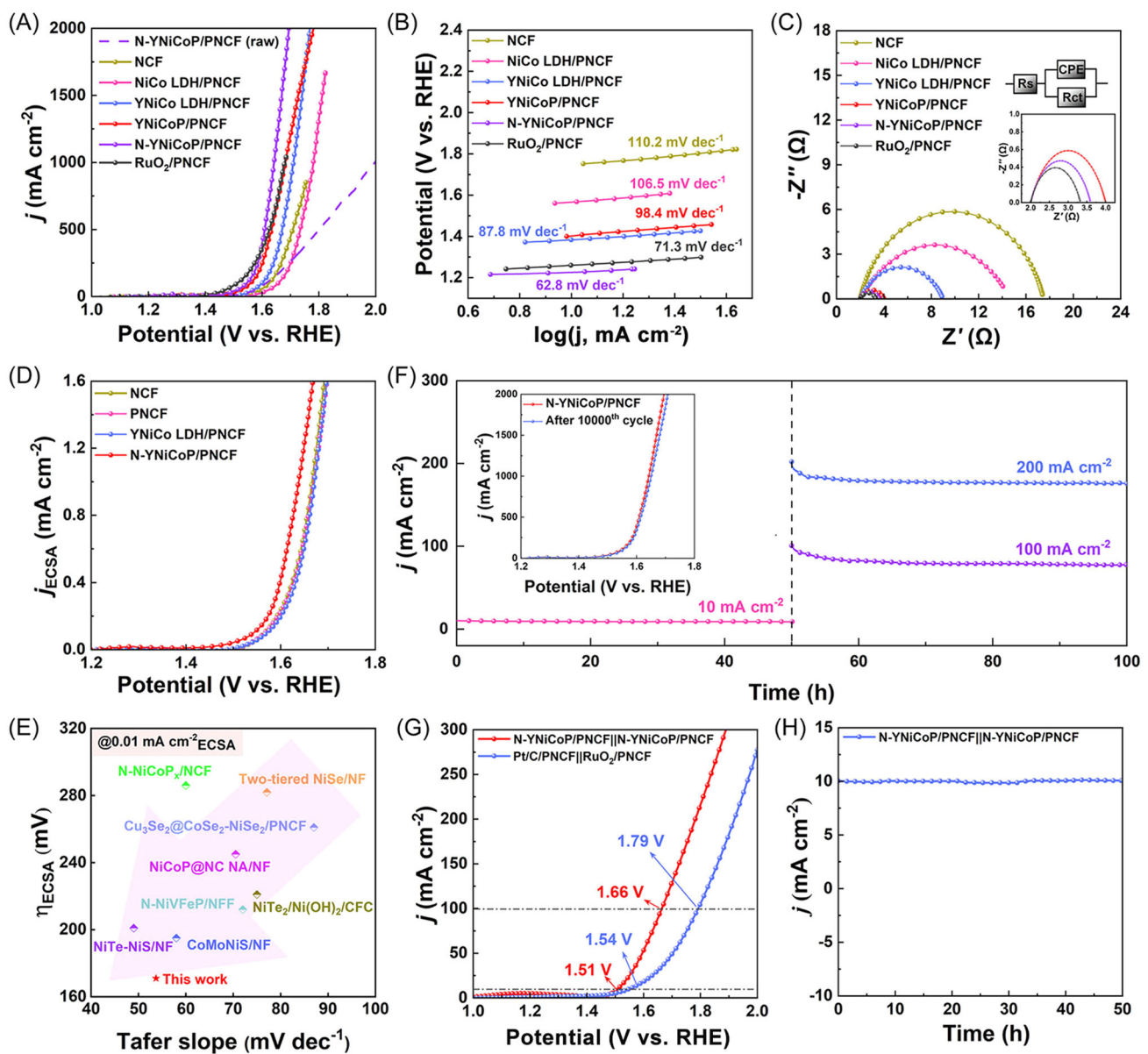


FIGURE 4 OER performance of different catalysts in 1.0 M KOH electrolyte. (A) Polarization curves, (B) Tafel slopes, (C) Nyquist plots, (D) OER curves of the catalysts normalized with the ECSA, (E) comparison of the overpotentials and Tafel slope at 0.01 mA cm⁻² normalized by ECSA with other state-of-the-art electrocatalysts, (F) chronoamperometric curves of N-YNiCoP/PNCF recorded at j_{10} , j_{100} , and j_{200} for 100 h and polarization curves of N-YNiCoP/PNCF before and after 10,000 cycles (inset), (G) polarization curves for the overall water electrolysis cell containing N-YNiCoP/PNCF||N-YNiCoP/PNCF and Pt/C/PNCF||RuO₂/PNCF catalysts, and (H) long-term stability of the N-YNiCoP/PNCF||N-YNiCoP/PNCF catalysts.

cycles provided in the inset of Figure 4F prove that N-YNiCoP/PNCF has excellent electrocatalytic durability/sustainability.

To assess the catalyst stability in the OER process, the morphology and chemical structures of N-YNiCoP after long-term OER current-time tests are also studied. As shown in Figure S35A,B, the nanosheet skeleton of N-YNiCoP is still preserved after the long-term OER test, except for the fact that smaller nanosheets are generated on the original surface, which may promote an increase

in OER activity. Figure S35C shows the elemental maps of the sample, and the Y, Ni, Co, O, P, and N elements are evenly distributed over the nanosheet surface. Figure S35D,E shows the TEM images of N-YNiCoP after the OER current-time tests, and the plane spacings of 0.221 and 0.203 nm associated with (210) and (201) planes of Co₂P and Ni₂P phases, respectively, still exist, as also confirmed by the SAED patterns (Figure S35F). It is noteworthy that the composition of the resulting tiny nanosheet is analyzed using an EDS line-scan protocol.

As can be seen from the data shown in Figure S35G,H, the small nanosheets are made of Ni, Co, and O atoms, and lower concentrations of Y, P, and N. These findings indicate that oxides or hydroxides are formed during the OER process. Figure S36 shows the XRD pattern of the catalyst before (red line) and after (purple line) the OER reaction. Interestingly, no new crystal phases appeared following the long-term OER reaction, except for NiOOH (JCPDS NO. 06-0075). However, some crystalline phases are lost, especially for the YP_5 phase, consistent with high-resolution TEM results. TEM-EDX (Figure S29C) and XPS (Table S1) data also indicate that some Y and P on the N-YNiCoP surface are consumed after the OER. Meanwhile, the content of O increases significantly, which may be caused by the catalyst oxidation.

Because of the demonstrated excellent HER and OER activities of the optimized catalyst, a N-YNiCoP/PNCF||N-YNiCoP/PNCF dual-electrode system is designed for overall water splitting. As shown in Figure 4G, the battery voltages for delivering j_{10} and j_{100} are, respectively, only 1.51 and 1.66 V, which are even better than those of the noble catalyst system of the Pt/C/PNCF||RuO₂/PNCF electrode (1.54 V/ j_{10} and 1.79 V/ j_{100}). Meanwhile, the cell voltage is lower compared to most recently reported high-quality catalysts (Table S10). Furthermore, a dual-function stability test is performed at j_{10} , as shown in Figure 4H, and the catalyst current does not change significantly over 50 h. The obtained results suggest that N-YNiCoP/PNCF indeed has excellent bifunctional electrocatalytic activity and stability.

3.4 | Quantum chemistry calculations

As shown in Figure 5A, to relate the N-YNiCoP structure and the observed high catalytic activity, DFT-based quantum chemistry computations are carried using the corresponding models of crystal structures. Hydrogen adsorption-free energy (ΔG_{H^*}) is commonly used to evaluate catalytic performance. Normally, a value of ΔG_{H^*} closer to zero indicates potentially better HER performance.¹⁷ Figure 5B shows the ΔG_{H^*} values of YP_5 , Co_2P , Ni_2P , CoN , CoN-YP_5 , $\text{CoN-Ni}_2\text{P}$, and $\text{Co}_2\text{P-Ni}_2\text{P}$, which correspond to 0.427, -1.716, -0.551, -1.319, -0.412, -0.495, and -1.189 eV, respectively. It is noteworthy that the N-doping and the formed heterogeneous interfaces obviously decrease the ΔG_{H^*} value, indicating that higher HER kinetics can be achieved. Specifically, the ΔG_{H^*} value of YP_5 is 0.427 eV, and it is only lower than that of the CoN-YP_5 interface, which is the main active site for HER, indicating that the phase mixture of YP_5 can effectively boost the catalytic activity. Meanwhile, the electron effects on the catalytic activity

are evaluated by the calculated density of states (DOS).⁹ As shown in Figure S37, since these phases all pass through the Fermi level (E_f), they all have metallic characteristics. Especially, the electronic DOS of $\text{CoN-Ni}_2\text{P}$ phase is higher around E_f than those of CoN and Ni_2P , which improves the H atom adsorption during HER. Besides, $\text{Co}_2\text{P-Ni}_2\text{P}$ and CoN-YP_5 show the same phenomenon, indicating that the electrical conductivity facilitates electron transport when heterogeneous interfaces are formed. This is consistent with the conclusions drawn from Figure 5B. Figures 5C and S38 show the d-band centers corresponding to different phases. For all the obtained results, d-band centers corresponding to the heterogeneous phases are farther away from the E_f than those of the single phases, indicating lower hydrogen adsorption energy.⁵⁰ Notably, as shown in Figure 5C, the d-band center value of CoN is -2.521 eV; however, it decreases to -2.581 eV when CoN forms a heterogeneous interface with YP_5 , indicating that the addition of Y effectively regulates the electronic structure and promotes electron transport, and is also useful for optimizing the hydrogen adsorption energy. In addition, the H_2O dissociation barrier of CoN-YP_5 (1.018 eV) is much lower than those of other active sites (Figure S39), suggesting that faster HER kinetics in alkaline media is achieved on the heterointerface of CoN-YP_5 .

As shown in Figure S40, we also determined the detailed OER mechanism using DFT calculations; the process is based on the 4e⁻ transfer reaction, which involves *OH, *O, and *OOH intermediate species.³⁷ Figures 5D and S41 reveal that the rate-determining steps are different for the obtained samples, but all the energy barriers of the formed heterostructures are lower than those for the corresponding single-phase materials. For example, the energy barriers of CoN-YP_5 , $\text{CoN-Ni}_2\text{P}$, and $\text{Co}_2\text{P-Ni}_2\text{P}$ are 0.478, 0.675, and 0.765 eV, respectively, which are much lower than those of the YP_5 (1.089 eV), CoN (1.032 eV), Ni_2P (1.109 eV), and Co_2P (0.866 eV) phases.

Based on the results of the above experimental and theoretical calculations, one can conclude that the incorporation of Y significantly boosts the activity in HER and OER, along with electrocatalytic stability. Meanwhile, the formed heterogeneous interface of CoN-YP_5 has the smallest energy barrier for both HER and OER processes, indicating that it is a major active interface in the catalytic process. Furthermore, plasma-enhanced N-doping can effectively increase the electron transfer rates and reduce the energy barrier of reactants' adsorption, thus promoting an increase in the catalytic activity for overall water splitting.¹⁰ Certainly, the other metal compounds (e.g., Ni_2P and Co_2P) engineered mainly support the frame structure of the catalyst and

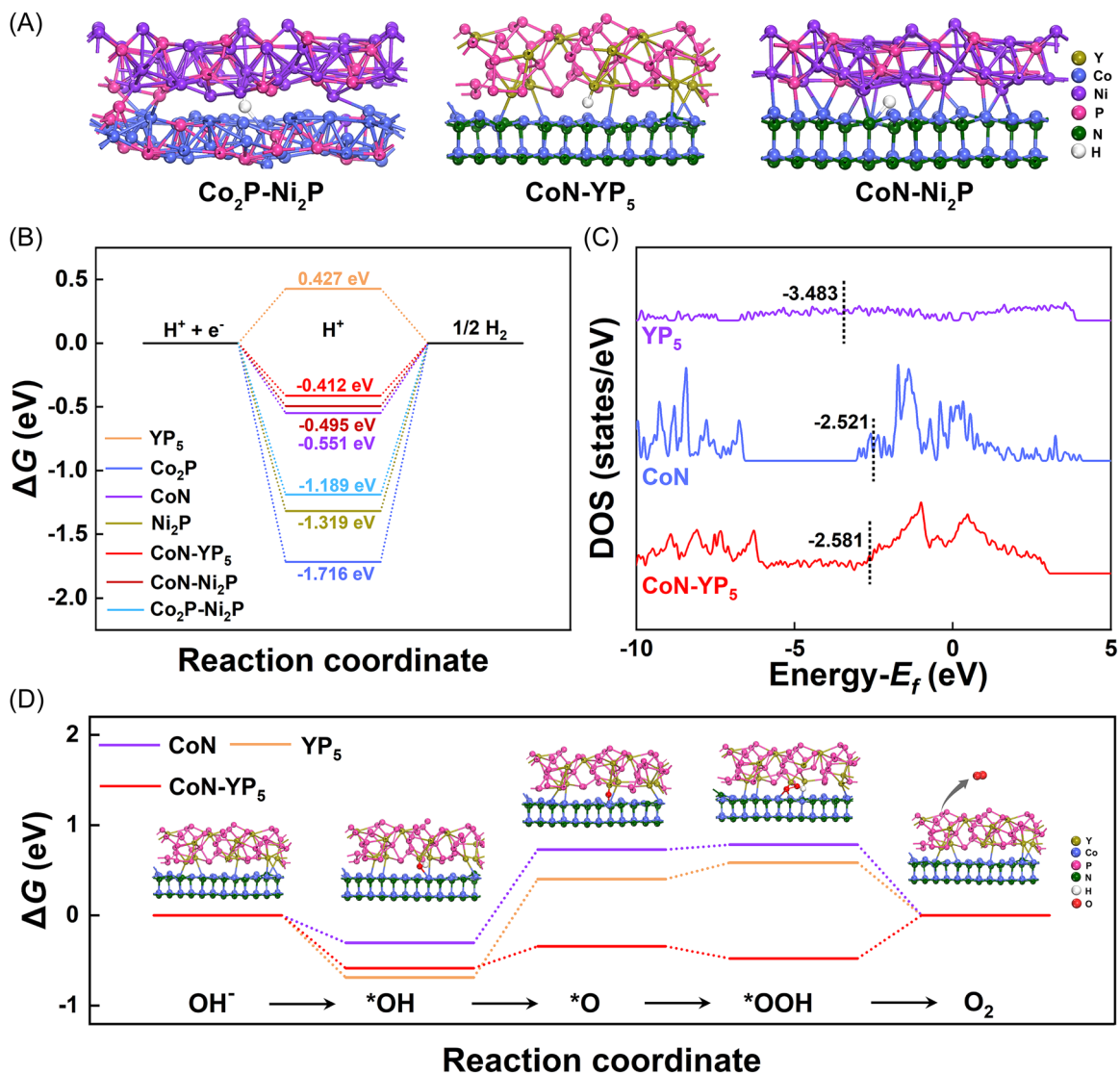


FIGURE 5 The ab initio DFT simulations reveal the mechanisms of the excellent catalytic activity and stability achieved. (A) Crystal structures of $\text{Co}_2\text{P}-\text{Ni}_2\text{P}$, $\text{CoN}-\text{YP}_5$, and $\text{CoN}-\text{Ni}_2\text{P}$ constructed based on the XRD and high resolution TEM results, (B) Gibbs free energies in the HER process, (C) d-band centers of YP_5 , CoN , and CoN-YP_5 , and (D) Gibbs free-energy evolution in the OER reaction steps (1.23 V) of YP_5 , CoN , and CoN-YP_5 .

contribute to tuning the crystal phases of $\text{N}-\text{YNiCoP}$. It should be noted that the newly formed NiOOH phase (Figure S36) after a long-term OER process helps maintain high electrocatalytic activity for $\text{N}-\text{YNiCoP}$ to generate O_2 in an alkaline medium.^{51,52}

4 | CONCLUSIONS

Here, we have revealed a new way to use a tiny amount of Y rare-Earth metal and plasma processing to markedly boost the electrocatalytic activity and stability under alkaline electrolysis conditions. Specifically, multiphase YNiCo phosphide nanosheets induced by the

incorporation of Y^{3+} ions were successfully synthesized, and the catalyst shows excellent catalytic activity and stability for both HER and OER in alkaline electrolytes. Structural characterization and electrochemical measurements indicate that the new catalyst has a very large active surface area and rich active centers, and enables fast electron transfer, which ensures superior performance to the catalysts based on noble metals under high and industry-relevant current densities. The XAS results show that the addition of Y atoms shortens the bond length and reduces the coordination numbers of Co and Ni atoms, which induce an increase in the interatomic binding energy and thus improves the stability of the synthesized catalysts. DFT-based quantum chemistry

calculations reveal that incorporation of Y atoms helps reduce the energy barrier of both HER and OER processes, resulting in faster reactive kinetics of N-YNiCoP/PNCF. Owing to the advantages of a self-supporting rigid structure, the catalyst activity is superior to that of noble-metal-based catalysts under high-current-density conditions. Notably, the HER and OER overpotentials required to yield j_{2000} are only 331 and 464 mV, respectively. Furthermore, the assembled N-YNiCoP/PNCF||N-YNiCoP/PNCF dual-electrode system shows excellent performance in water electrolysis. The demonstrated performance is notably better than that for the cell assembled with a noble Pt/C/PNCF||RuO₂/PNCF electrode and a few recently reported high-quality catalysts. Importantly, this new approach for engineering electrocatalysts using small amounts of rare-earth metals is generic and is highly promising for the production of H₂ and O₂ at large, industry-relevant scales by water electrolysis and other commercial applications of electrocatalysis.

ACKNOWLEDGEMENTS

The authors acknowledge support from the National Natural Science Foundation of China (52177162), the Natural Science Foundation of Zhejiang Province (LZ22E070003 and LQ22E020006), the Funding Project for Academic/Technical Leaders of Jiangxi Province (20225BCJ22003), and the Natural Science Foundation of Jiangxi Province (20212ACB211001). Kostya (Ken) Ostrikov appreciates partial support from the Australian Research Council and Centre for Materials Science (QUT).

CONFLICT OF INTEREST STATEMENT

The authors declare that there are no conflicts of interests.

ORCID

Guangliang Chen  <http://orcid.org/0000-0002-8556-1741>

Tongtong Li  <http://orcid.org/0000-0003-1165-1573>

REFERENCES

1. Wang Y, Li X, Zhang M, et al. Highly active and durable single-atom tungsten-doped NiS_{0.5}Se_{0.5} nanosheet@NiS_{0.5}Se_{0.5} nanorod heterostructures for water splitting. *Adv Mater*. 2022;34(13):2107053.
2. Yang Y, Zhang W, Xiao Y, et al. CoNiSe₂ heteronanorods decorated with layered-double-hydroxides for efficient hydrogen evolution. *Appl Catal B*. 2019;242:132-139.
3. Wang J, Huang J, Chen G, et al. In-situ engineered heterostructured nickel tellur-selenide nanosheets for robust overall water splitting. *Chem Eng J*. 2022;446:137297.
4. Liang Z, Yin L, Yin H, Yin Z, Du Y. Rare earth element based single-atom catalysts: synthesis, characterization and applications in photo/electro-catalytic reactions. *Nanoscale Horiz*. 2022;7(1):31-40.
5. Li GR, Liu M, Wang HM, et al. Effect of the rare earth element yttrium on the structure and properties of boron-containing high-entropy alloy. *JOM*. 2020;72(6):2332-2339.
6. Yang J, Li X, Cheng Y, et al. Efficient and selective aqueous photocatalytic mono-dehydration of sugar alcohols using functionalized yttrium oxide nanocatalysts. *Green Chem*. 2020;22(16):5333-5344.
7. Zhang S, Saji SE, Yin Z, Zhang H, Du Y, Yan CH. Rare-earth incorporated alloy catalysts: synthesis, properties, and applications. *Adv Mater*. 2021;33(16):2005988.
8. Jiang H, Sun M, Wu S, Huang B, Lee CS, Zhang W. Oxygen-incorporated NiMoP nanotube arrays as efficient bifunctional electrocatalysts for urea-assisted energy-saving hydrogen production in alkaline electrolyte. *Adv Funct Mater*. 2021;31(43):2104951.
9. Fan H, Chen W, Chen G, et al. Plasma-heteroatom-doped Ni-V-Fe trimetallic phospho-nitride as high-performance bifunctional electrocatalyst. *Appl Catal B*. 2020;268:118440.
10. Jin R, Huang J, Chen G, et al. Water-sprouted, plasma-enhanced Ni-Co phospho-nitride nanosheets boost electrocatalytic hydrogen and oxygen evolution. *Chem Eng J*. 2020;402:126257.
11. Surendran S, Shanmugapriya S, Sivanantham A, Shanmugam S, Kalai Selvan R. Electrospun carbon nanofibers encapsulated with NiCop: a multifunctional electrode for supercapattery and oxygen reduction, oxygen evolution, and hydrogen evolution reactions. *Adv Energy Mater*. 2018;8(20):1800555.
12. Zhang XY, Zhu YR, Chen Y, et al. Hydrogen evolution under large-current-density based on fluorine-doped cobalt-iron phosphides. *Chem Eng J*. 2020;399:125831.
13. Jiang N, Zhuo X, Wang J. Active plasmonics: principles, structures, and applications. *Chem Rev*. 2017;118(6):3054-3099.
14. Chen D, Xu Z, Chen W, et al. Mulberry-inspired nickel-niobium phosphide on plasma-defect-engineered carbon support for high-performance hydrogen evolution. *Small*. 2020;16(43):2004843.
15. Liang H, Ming F, Alshareef HN. Applications of plasma in energy conversion and storage materials. *Adv Energy Mater*. 2018;8(29):1801804.
16. Xiao Z, Wang Y, Huang YC, et al. Filling the oxygen vacancies in Co₃O₄ with phosphorus: an ultra-efficient electrocatalyst for overall water splitting. *Energy Environ Sci*. 2017;10(12):2563-2569.
17. Shen S, Wang Z, Lin Z, et al. Crystalline-amorphous interfaces coupling of CoSe₂/CoP with optimized d-band center and boosted electrocatalytic hydrogen evolution. *Adv Mater*. 2022;34(13):2110631.
18. Wang G, Chen W, Chen G, et al. Trimetallic Mo-Ni-Co selenides nanorod electrocatalysts for highly-efficient and ultra-stable hydrogen evolution. *Nano Energy*. 2020;71:104637.
19. Liu H, Guan J, Yang S, et al. Metal-organic-framework-derived Co₂P nanoparticle/multi-doped porous carbon as a trifunctional electrocatalyst. *Adv Mater*. 2020;32(36):2003649.
20. Wen S, Huang J, Li T, et al. Multiphase nanosheet-nanowire cerium oxide and nickel-cobalt phosphide for highly-efficient

- electrocatalytic overall water splitting. *Appl Catal B*. 2022; 316:121678.
- 21. Wen S, Chen G, Chen W, et al. Nb-doped layered FeNi phosphide nanosheets for highly efficient overall water splitting under high current densities. *J Mater Chem A*. 2021;9(15):9918-9926.
 - 22. Qu S, Huang J, Yu J, et al. Ni₃S₂ nanosheet flowers decorated with CdS quantum dots as a highly active electrocatalysis electrode for synergistic water splitting. *ACS Appl Mater Interfaces*. 2017;9(35):29660-29668.
 - 23. Zhong C, Han Z, Wang T, et al. Aliovalent fluorine doping and anodization-induced amorphization enable bifunctional catalysts for efficient water splitting. *J Mater Chem A*. 2020;8(21): 10831-10838.
 - 24. Chen G, Chen D, Huang J, et al. Focused plasma-and pure water-enabled, electrode-emerged nanointerfaced nico hydroxide–oxide for robust overall water splitting. *ACS Appl Mater Interfaces*. 2021;13(38):45566-45577.
 - 25. Qin Z, Wang X, Dong L, et al. CO₂ methanation on Co/TiO₂ catalyst: effects of Y on the support. *Chem Eng Sci*. 2019; 210:115245.
 - 26. Zheng YR, Wu P, Gao MR, et al. Doping-induced structural phase transition in cobalt diselenide enables enhanced hydrogen evolution catalysis. *Nat Commun*. 2018;9(1):2533.
 - 27. Song H, Li Y, Shang L, Tang Z, Zhang T, Lu S. Designed controllable nitrogen-doped carbon-dots-loaded MoP nanoparticles for boosting hydrogen evolution reaction in alkaline medium. *Nano Energy*. 2020;72:104730.
 - 28. Zhang R, Huang J, Chen G, et al. In situ engineering bimetallic phospho-nitride bi-functional electrocatalysts for overall water splitting. *Appl Catal B*. 2019;254:414-423.
 - 29. Najam T, Shoaib Ahmad Shah S, Sufyan Javed M, et al. Modulating the electronic structure of zinc single atom catalyst by P/N coordination and Co₂P supports for efficient oxygen reduction in Zn-air battery. *Chem Eng J*. 2022;440:135928.
 - 30. Zhao Y, Dongfang N, Triana CA, et al. Dynamics and control of active sites in hierarchically nanostructured cobalt phosphide/chalcogenide-based electrocatalysts for water splitting. *Energy Environ Sci*. 2022;15(2):727-739.
 - 31. Xu YF, Duchesne PN, Wang L, et al. High-performance light-driven heterogeneous CO₂ catalysis with near-unity selectivity on metal phosphides. *Nat Commun*. 2020;11(1):5149.
 - 32. Hou CC, Li Q, Wang CJ, et al. Ternary Ni-Co-P nanoparticles as noble-metal-free catalysts to boost the hydrolytic dehydrogenation of ammonia-borane. *Energy Environ Sci*. 2017;10(8):1770-1776.
 - 33. Wang Q, Zhang Z, Cai C, et al. Single iridium atom doped Ni₂P catalyst for optimal oxygen evolution. *J Am Chem Soc*. 2021;143(34):13605-13615.
 - 34. Finck N, Bouby M, Dardenne K, Yokosawa T. Yttrium coprecipitation with smectite: A polarized XAS and AsFlFFF study. *Appl Clay Sci*. 2017;137:11-21.
 - 35. Kim M, Lee B, Ju H, Lee SW, Kim J. Reducing the barrier energy of self-reconstruction for anchored cobalt nanoparticles as highly active oxygen evolution electrocatalyst. *Adv Mater*. 2019;31(32):1901977.
 - 36. Liu B, Zhao YF, Peng HQ, et al. Nickel–cobalt diselenide 3D mesoporous nanosheet networks supported on Ni foam: an all-pH highly efficient integrated electrocatalyst for hydrogen evolution. *Adv Mater*. 2017;29(19):1606521.
 - 37. Li X, Wang Y, Wang J, et al. Sequential electrodeposition of bifunctional catalytically active structures in MoO₃/Ni–NiO composite electrocatalysts for selective hydrogen and oxygen evolution. *Adv Mater*. 2020;32(39):2003414.
 - 38. Zheng Z, Yu L, Gao M, et al. Boosting hydrogen evolution on MoS₂ via co-confining selenium in surface and cobalt in inner layer. *Nat Commun*. 2020;11(1):3315.
 - 39. Liu W, Wang X, Wang F, et al. A durable and pH-universal self-standing MoC–Mo₂C heterojunction electrode for efficient hydrogen evolution reaction. *Nat Commun*. 2021;12(1):6776.
 - 40. Sunny A, Balasubramanian K. Laser-induced phonon and magnon properties of NiO nanoparticles: a Raman study. *J Raman Spectrosc*. 2021;52(4):833-842.
 - 41. Faid AY, Barnett AO, Seland F, Sunde S. Ni/NiO nanosheets for alkaline hydrogen evolution reaction: in situ electrochemical-Raman study. *Electrochim Acta*. 2020;361:137040.
 - 42. Zhang W, Desorme C, Valverde JL, Giroir-Fendler A. Yttrium-modified Co₃O₄ as efficient catalysts for toluene and propane combustion: effect of yttrium content. *J Hazard Mater*. 2022;437:129316.
 - 43. Deng L, Hu F, Ma M, et al. Electronic modulation caused by interfacial Ni–O–M (M = Ru, Ir, Pd) bonding for accelerating hydrogen evolution kinetics. *Angew Chem Int Ed*. 2021;60(41): 22276-22282.
 - 44. Yang Y, Yao H, Yu Z, et al. Hierarchical nanoassembly of MoS₂/Co₉S₈/Ni₃S₂/Ni as a highly efficient electrocatalyst for overall water splitting in a wide pH range. *J Am Chem Soc*. 2019;141(26):10417-10430.
 - 45. Xue Z, Li X, Liu Q, et al. Interfacial electronic structure modulation of NiTe nanoarrays with NiS nanodots facilitates electrocatalytic oxygen evolution. *Adv Mater*. 2019;31(21): 1900430.
 - 46. Xu B, Yang X, Liu X, et al. Lattice distortion in hybrid NiTe₂/Ni(OH)₂ nanosheets as efficient synergistic electrocatalyst for water and urea oxidation. *J Power Sources*. 2020; 449:227585.
 - 47. Cao B, Cheng Y, Hu M, et al. Efficient and durable 3D self-supported nitrogen-doped carbon-coupled nickel/cobalt phosphide electrodes: stoichiometric ratio regulated phase-and morphology-dependent overall water splitting performance. *Adv Funct Mater*. 2019;29(44):1906316.
 - 48. Wang G, Huang J, Chen G, et al. In-situ-engineered 3D Cu₃Se₂@ CoSe₂-NiSe₂ nanostructures for highly efficient electrocatalytic water splitting. *ACS Sustainable Chem Eng*. 2020;8(46):17215-17224.
 - 49. Wu H, Lu X, Zheng G, Ho GW. Topotactic engineering of ultrathin 2D nonlayered nickel selenides for full water electrolysis. *Adv Energy Mater*. 2018;8(14):1702704.
 - 50. Hu Q, Gao K, Wang X, et al. Subnanometric Ru clusters with upshifted D band center improve performance for alkaline hydrogen evolution reaction. *Nat Commun*. 2022;13(1):3958.
 - 51. Li T, Yu Y, Pei M. Dual-atom doping carbon materials as highly efficient electrocatalysts for lithium-sulfur batteries: bimetallic cooperation mechanism. *J Phys Chem C*. 2023; 127(13):6271-6279.
 - 52. Yan F, Zhu C, Li C, Zhang S, Zhang X, Chen Y. Highly stable three-dimensional nickel–iron oxyhydroxide catalysts for

oxygen evolution reaction at high current densities.
Electrochim Acta. 2017;245:770-779.

SUPPORTING INFORMATION

Additional supporting information can be found online in the Supporting Information section at the end of this article.

How to cite this article: Chen G, Xiang H, Guo Y, et al. Yttrium- and nitrogen-doped NiCo phosphide nanosheets for high-efficiency water electrolysis. *Carbon Energy*. 2024;6:e522.
[doi:10.1002/cey2.522](https://doi.org/10.1002/cey2.522)